

Cavity Plasmonics in Tunnel Junctions: Outcoupling and the Role of Surface Roughness

Thorin J. Duffin,^{1,2} Vijith Kalathingal,^{2,3,*} Andreea Radulescu,² Changjian Li,⁴ Stephen J. Pennycook,⁴ and Christian A. Nijhuis^{1,2,3,†}

¹*National University of Singapore Graduate School for Integrative Sciences and Engineering, National University of Singapore, 28 Medical Drive, Singapore 117456, Singapore*

²*Department of Chemistry, National University of Singapore, 3 Science Drive, Singapore 117543, Singapore*

³*Centre for Advanced 2D Materials and Graphene Research Centre, National University of Singapore, 6 Science Drive 2, Singapore 117564, Singapore*

⁴*Department of Material Science & Engineering, National University of Singapore, 9 Engineering Drive 1, Singapore 117575, Singapore*



(Received 28 May 2020; revised 26 August 2020; accepted 31 August 2020; published 14 October 2020)

Electrical excitation of surface plasmons via metal-insulator-metal tunneling junctions (*M-I-M* TJs) has recently been demonstrated to have experimental conversion efficiencies of 1% [W. Du *et al.* Nat. Photonics 11, 623 (2017)], 5–6 orders of magnitude higher than theoretically predicted by Parzefall and Novotny [ACS Photonics 5, 4195 (2018)]. In this work we resolve this discrepancy between theory and experiment, and report a rigorous analytical and experimental study on the role of surface roughness in the near-field coupling of the initially excited *M-I-M* TJ cavity surface plasmon polariton (*M-I-M* SPP) to the daughter radiative and nonradiative modes. We find that varying the roughness profile of the *M-I-M* TJ significantly (which is determined with atomic force microscopy and cross-section scanning transmission electron microscopy) improves the near-field outcoupling efficiency for two reasons: the effective thickness of the electrodes reduces with increasing roughness, and roughness provides momentum matching for mode overlap. The role of surface roughness in near-field outcoupling is analysed quantitatively by incorporating a conformal random roughness profile in the finite-element electromagnetic modeling of a plasmonically active *M-I-M* TJ. We show that the outcoupling efficiency can be enhanced up to 15% for the *M-I-M* SPP coupling to daughter modes, and demonstrate an overall electron-to-plasmon conversion efficiency of 1.5% (based on an inelastic tunneling efficiency of 10%), supporting recent experimental findings. This work provides an explanation for the high observed experimental efficiencies and bridges the knowledge gap between prior theoretical works and experiments by including the role of roughness in the electromagnetic near-field coupling in *M-I-M* TJs.

DOI: 10.1103/PhysRevApplied.14.044021

I. INTRODUCTION

Metal-insulator-metal tunnel junctions (*M-I-M* TJs) can excite—by inelastic electron tunneling—surface plasmon polaritons (SPPs) and photons under an applied bias [3–6]. Therefore, *M-I-M* TJs offer (potentially) complementary functionality across a myriad of applications in sensing [7–9], nano-optics [1,10,11], and nonlinear plasmonics [12,13]. However, there remains a large discrepancy in the literature over experimentally reported overall electron-to-SPP excitation efficiencies—especially in large area, nonresonant *M-I-M* TJs (1%) [1]—and those theoretically calculated by Parzefall *et al.* (10^{-8}) [2]. Later, Qian *et al.* reported 2% free-space photon emission efficiencies from

plasmonically resonant junctions based on Ag nanocubes [14]. This discrepancy between theory and experiment needs to be addressed to deepen our understanding of light-matter interactions in plasmonic tunneling junctions and to continue to explore their potential.

Light emission and SPP excitation from *M-I-M* TJs under applied bias is a well-known phenomenon that has been extensively explored [1,3,4,6,15]. Initially, an electron inelastically tunnels through the dielectric tunneling barrier between two electrodes and couples a fraction of its energy to various decay channels defined by the local density of optical states (LDOS). *M-I-M* TJs can excite the *M-I-M* TJ cavity mode (*M-I-M* SPP), which outcouples to radiative and nonradiative modes, as well as directly excites photons and single-interface SPPs [16–20]. These two phenomena are usually examined separately: (i) exploration of cavity-mode excitation via

*c2dvika@nus.edu.sg

†christian.nijhuis@nus.edu.sg

tunneling [20,21], and (ii) single-interface SPP and/or photon outcoupling via surface modification in the far field [4,15,22–25]. Examining the role of the *M-I-M* TJ in the near-field interaction between the highly confined, non-radiative *M-I-M* SPP mode and the local topographical features—combining (i) and (ii)—has not been examined in detail, due to the complexity in analytically studying nanoscale interactions with statistically meaningful *M-I-M* TJ topographies.

This paper quantifies the pivotal role that the surface roughness of the electrode materials plays in the outcoupling of the *M-I-M* SPP mode to daughter modes. Theoretically, the internal quantum efficiency of *M-I-M* TJs for the excitation of *M-I-M* SPPs is limited to 10% (because of the presence of various radiative and nonradiative decay channels) [5], which is the upper limit for total electron-to-plasmon conversion efficiency. However, in planar *M-I-M* TJs (where the insulator usually has a thickness of only 2–3 nm) with a smooth interface, the outcoupling efficiency is predicted to be $< 10^{-6}$ due to the large momentum mismatch between the *M-I-M* SPP and daughter modes [2,23], but recent experimental works with inherent electrode roughness report outcoupling efficiencies 4 orders of magnitude higher [1,6].

To date, it is not clear how such a high outcoupling of the *M-I-M* SPP efficiency to single interface propagating SPPs and photons can be achieved given the highly confined nature of the *M-I-M* SPP mode. Due to this confinement, the propagation length of the *M-I-M* SPP mode is of the order of a few tens of nanometres (see Sec. S1 within the Supplemental Material [26]). For this reason, Parzefall *et al.* [2] argued that in smooth, large-area *M-I-M* TJs, the only efficient outcoupling of the mode can take place at the *M-I-M* TJ edges. Recently, we [6] have demonstrated three efficient outcoupling channels that can be controlled by electrode thickness, and suggested that roughness in the electrode materials is important to provide momentum matching and associated *M-I-M* SPP mode scattering, resulting in an increase of the outcoupling efficiencies by at least 2 orders of magnitude higher than previously suggested [2,23]. Here we report an analytical model, supported by experimental data, for plasmon outcoupling in *M-I-M* TJs predicated on incorporating surface roughness of the electrode into electromagnetic mode scattering, and show that this can lead to up to 15% outcoupling efficiency of the *M-I-M* SPP mode (limited by losses in the electrode) and therefore an overall excitation and outcoupling efficiency of up to 1.5%, supporting our recent experimental results [1].

Using surface modification to increase light-emission intensity from *M-I-M* TJs is a known technique that facilitates exploration of the spectral properties of different modes by statistical (random) roughening [1,6,15,27–37], grating patterning [38–42], and prism outcoupling [25,36,43,44]. In these studies, light emission from *M-I-M* TJs

is typically investigated in the far field where the role of roughness in near-field outcoupling is ignored, although roughness is known to be a crucial factor in single-interface systems [45]. Roughness is always inherently present in interfaces due to grains and grain boundaries, ad atoms, step edges, and other types of defects, except for a few systems where atomically smooth interfaces can be fabricated only under extremely well-controlled conditions [46,47]. Moreover, in designed rough topographies that can support picocavities, coherent physical effects can be exploited to further amplify near-field phenomena [48,49], whereas other surface-plasmon-based technologies like surface-enhanced Raman spectroscopy (SERS) exploit surface roughness to increase near-field signal intensity [50]. However, the role of surface roughness in *M-I-M* TJs in the near field and the near-field coupling to both radiative and nonradiative modes remains so far unexplored and this is the main focus of this work.

II. RESULTS AND DISCUSSION

A. Theory

1. SPP excitation in smooth *M-I-M* TJs

When a voltage is applied across two electrodes separated by a dielectric of 1–3 nm in thickness, electrons will tunnel elastically and inelastically across the tunneling barrier, with inelastic tunneling represented in the energy-level diagram in Fig. 1(a) with a white arrow, where the energy difference from the applied voltage eV is the difference between the Fermi energy of the Au ($\varepsilon_f^{\text{Au}}$) and Al ($\varepsilon_f^{\text{Al}}$), and the inelastic tunneling energy loss is given as $\hbar\omega$. The heatmap in Fig. 1(a) shows the symmetric mode profile of the *M-I-M* SPP (normalized electromagnetic field intensity) highly confined within the insulator, obtained from the two-dimensional- (2D) mode analysis of the smooth *M-I-M* TJ using COMSOL Multiphysics 5.1 [51]. Here we discuss SPP excitation in ideally smooth junctions, and in the next section we include surface roughness in our model.

Inelastic tunneling is modeled using an oscillating electric current dipole, which is used as the excitation source for the *M-I-M* SPP. In the time harmonic limit an oscillating point dipole $\mu e^{-i\omega t}$ located at a point \mathbf{r}_0 is equivalent to a line current density $\mathbf{j}(\mathbf{r})$ [52]:

$$\mathbf{j}(\mathbf{r}) = -i\omega\mu\delta(\mathbf{r} - \mathbf{r}_0), \quad (1)$$

where μ is the amplitude of the dipole oscillation, ω is the angular frequency and $\delta(\mathbf{r} - \mathbf{r}_0)$ is the Dirac delta function.

From the angular representation of the electromagnetic fields, the electric $\mathbf{E}(\mathbf{r})$ and magnetic $\mathbf{B}(\mathbf{r})$ fields can be represented as a superposition of plane waves and evanescent waves: $\mathbf{E}(\mathbf{r}) = \int d\mathbf{k}\mathbf{E}_k \exp(i\mathbf{k} \cdot \mathbf{r})$ and $\mathbf{B}(\mathbf{r}) = \int d\mathbf{k}\mathbf{B}_k \exp(i\mathbf{k} \cdot \mathbf{r})$, where \mathbf{E}_k and \mathbf{B}_k represent the Fourier amplitude of the electric and magnetic field, respectively.

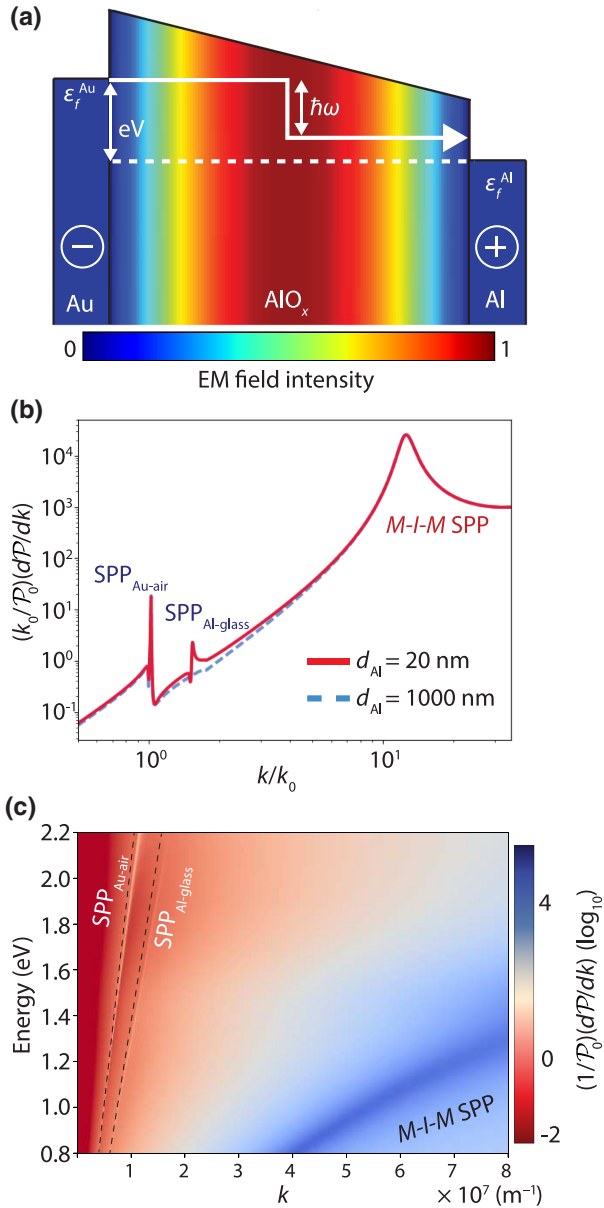


FIG. 1. (a) Energy-level diagram of the *M-I-M* TJ with the normalized electromagnetic field intensity indicated, (b) $(k_0/\mathcal{P}_0)(d\mathcal{P}/dk)$ [Eq. (3)] evaluated for a flat Au- AlO_x -Al junction for thick ($d_{\text{Al}} = 1000 \text{ nm}$; red solid line) and thin ($d_{\text{Al}} = 20 \text{ nm}$; blue dashed line) Al electrode; $d_{\text{Au}} = 20 \text{ nm}$, $\lambda_d = 900 \text{ nm}$. (c) $(1/\mathcal{P}_0)(d\mathcal{P}/dk)$ [Eq. (3)] evaluated as a function of energy and k , representing the dispersion of the supported plasmonic modes for an air-Au- AlO_x -Al-glass system ($d_{\text{Au}} = 20 \text{ nm}$, $d_{\text{AlO}_x} = 2 \text{ nm}$ and $d_{\text{Al}} = 20 \text{ nm}$). The dashed lines represent the light dispersion for the corresponding dielectric medium (air and glass).

The power dissipation spectrum \mathcal{P} can be used to obtain the plasmonic mode dispersion from the dipole model [53]:

$$\mathcal{P} = \frac{\omega}{2} \text{Im}(\boldsymbol{\mu}^* \cdot \mathbf{E}), \quad (2)$$

where $\boldsymbol{\mu}^*$ gives the complex conjugate of $\boldsymbol{\mu}$ and retardation effects are neglected in the calculations [54]. From Eq. (2) the k -space power-dissipation spectrum is defined as the integral of the dipole power dissipation $d\mathcal{P}/dk$ over all in-plane wave vectors k :

$$\mathcal{P} = \int_0^\infty dk \left(\frac{d\mathcal{P}}{dk} \right), \quad (3)$$

which can be decomposed into $\mathcal{P} = \mathcal{P}_{\text{photon}} + \mathcal{P}_{\text{SPP}} + \mathcal{P}_{\text{NR}}$, where $\mathcal{P}_{\text{photon}}$, \mathcal{P}_{SPP} , and \mathcal{P}_{NR} represent the dipole power dissipated into photons, SPPs, and nonradiative and thermal decay, respectively. The power dissipation of a vertically oriented dipole (normal to the *M-I-M* TJ interface), representing the normalized decay rate \mathcal{P}' , can be written as [53]

$$\mathcal{P}' = \frac{3}{2} \text{Re} \int_0^\infty dk \frac{k^3}{k_0^3 q_i} \left[\frac{(1 + d_{\downarrow}^p)(1 + d_{\uparrow}^p)}{1 - (d_{\uparrow}^p \times d_{\downarrow}^p)} \right], \quad (4)$$

where $d_{\uparrow,\downarrow}^p$ represents the effective field amplitude at the dipole's position, $k_0 = \omega/c$, $q_i = \sqrt{k_i^2 - k^2}$ and $k_i = (\omega/c)\sqrt{\varepsilon_i}$ with ε_i representing the permittivity of the insulator where the dipole is located (see Sec. S2 within the Supplemental Material for details [26]). Figures 1(b) and 1(c) show energy-dependent power-dissipation spectra, which gives the dispersion of the supported plasmonic modes for a smooth (no roughness) Au- AlO_x -Al *M-I-M* TJ. Figure 1(b) gives $(k_0/\mathcal{P}_0)(d\mathcal{P}/dk)$ [normalized integrand of Eq. (3)], where \mathcal{P}_0 is the free-space LDOS] evaluated for a flat Au- AlO_x -Al *M-I-M* TJ with a thick ($d_{\text{Al}} = 1000 \text{ nm}$, blue dashed line) and thin ($d_{\text{Al}} = 20 \text{ nm}$, red line) Al electrode, for a given Au electrode thickness $d_{\text{Au}} = 20 \text{ nm}$. Figure 1(b) is evaluated at excitation wavelength $\lambda_d = 900 \text{ nm}$ and k_0 represents the free-space wave number corresponding to λ_d . The Au electrode is bounded above by air with refractive index $n_{\text{air}} = 1$ and Al electrode from below by glass where $n_{\text{glass}} = 1.52$.

The broad peak at normalized wave number $k/k_0 \approx 10$ corresponds to the *M-I-M* SPP mode, which represents the predominant plasmonic decay channel for the energy from the inelastically tunneling electrons. When the Al electrode thickness d_{Al} is much larger than the skin depth Λ_{Al} , excitation of the single-interface SPP mode ($\text{SPP}_{\text{Al-glass}}$, $k/k_0 \approx 1.52$) is completely absent due to the large electromagnetic screening [Fig. 1(b), blue dashed line] in the Al electrode. When d_{Al} becomes comparable to Λ_{Al} [55], coupling to the $\text{SPP}_{\text{Al-glass}}$ is observed [Fig. 1(b), red line, narrow peak at $k/k_0 \approx 1.52$] [4,38,56]. In both cases, coupling to the Au-air SPP mode ($\text{SPP}_{\text{Au-air}}$) is observed at $k/k_0 \approx 1$ since the thickness of the Au electrode used in the calculation ($d_{\text{Au}} = 20 \text{ nm}$) is comparable to skin depth of Au [57]. Integrating the area under each peak in Fig. 1(b)

gives the corresponding LDOS for the given energy (1.37 eV \equiv 900 nm).

Evaluating $(1/\mathcal{P}_0)(d\mathcal{P}/dk)$ for the broadband energy range (0.8 to 2.2 eV) gives the dispersion relation for the smooth *M-I-M* TJ [Fig. 1(c)]. The dotted lines represent the light dispersion for the corresponding dielectric media (air and glass). The large momentum mismatch in the LDOS between the single-interface SPP modes ($1 < k/k_0 < 1.52$) and photonic band ($k/k_0 < 1$) with the *M-I-M* SPP mode ($k/k_0 \approx 10$) is evident from the dispersion relation [Fig. 1(c)]. Also, the coupling strength of the dipole energy to $\mathcal{P}_{\text{photon}}$, \mathcal{P}_{SPP} , and \mathcal{P}_{NR} can be qualitatively understood from the intensity of each mode in the dispersion relation. The relative coupling strength of the *M-I-M* SPP mode is 4–5 orders of magnitude higher than to SPP modes or photons. It is important to note that the large normalized LDOS (approximately equal to $10^4 - 10^5$) associated with the *M-I-M* SPP mode is highly confined within the insulator layer and, without the presence of surface features to assist in momentum matching the *M-I-M* SPP, we calculate similar outcoupling efficiencies to Parzefall *et al.* [2]. In contrast, in the presence of surface features, a near-field interaction between the *M-I-M* SPP and the roughness can induce momentum matching via scattering, significantly increasing the *M-I-M* SPP outcoupling efficiency as shown in the next section.

2. Surface roughness

Interface inhomogeneity is parametrized by surface roughness. Surface roughness is a broad term that can be measured by various methods, but here we examine 2D surfaces, which can be described meaningfully with the statistical rms roughness δ_q . In a 2D system, the surface can be divided into regions of local height variation (local peak-to-valley roughness). These regions of local height variation can then be averaged across the entire surface to create a statistical distribution of the roughness of the film. Due to the random nature of the grain size distribution in the metal film, the film topography can be realistically described with a Gaussian distribution; these statistical features can then be incorporated into an analytical model and used to calculate modifications to the electromagnetic nature of the system induced by roughness and their effect on outcoupling behaviors of the SPP modes.

Roughness can be considered as a perturbation $\xi(x, y)$ to a smooth planar surface from a height $r(x_0, y_0)$ given by the surface topographical function $\xi(x, y)$ [22,58,59]:

$$\xi(x, y) = r(x_0, y_0) + \xi(x, y) \quad (5)$$

such that $\langle \xi(x, y) \rangle = r(x_0, y_0)$.

The statistical character of the roughness along the electrode surface is implemented by the correlation function

defined as $\langle \xi(x)|\xi(x+x') \rangle$. For a typical Gaussian correlation

$$\langle \xi(x)|\xi(x+x') \rangle = \delta_q^2 \exp \left[\frac{-|x-x'|^2}{\sigma^2} \right], \quad (6)$$

where the transverse correlation length σ and δ_q is given by the average of n samples of $\xi(x, y)$:

$$\delta_q = \sqrt{\frac{1}{n} \sum_{xy} \xi(x, y)^2}, \quad (7)$$

$$\sigma = \sum_{xy} \xi(x, y) \times \xi(x', y'). \quad (8)$$

The presence of surface roughness on the electrodes causes a change in the electromagnetic attenuation compared to if the interface was smooth. This change in attenuation can be defined an effective thickness d_{eff} in terms of δ_q and σ as [60]

$$d_{\text{eff}} = d_m - 3\sqrt{\pi} \frac{\delta_q^2}{\sigma}, \quad (9)$$

where $d_m = d_{\text{Al}}$ or d_{Au} . Physically, this results in regions of higher electromagnetic attenuation and regions of lower attenuation as the thickness profile varies, which has a significant influence on the overall outcoupling of the *M-I-M* SPP.

3. Role of roughness on outcoupling pathways

For large-area *M-I-M* TJs where both electrodes are plasmonically active within the same wavelength range, the *M-I-M* SPP mode is the main plasmonic decay pathway other than energy dissipation into the lattice (Fig. 2, indicated in red). The *M-I-M* SPP can then outcouple to various radiative (Fig. 2, indicated in green) or nonradiative (Fig. 2, indicated in blue) modes through momentum matching, which is facilitated by the near-field interactions with the surface features. *M-I-M* SPP outcoupling to daughter electromagnetic modes in *M-I-M* TJs can occur via three pathways that we have recently reported [6] (Fig. 2): direct outcoupling via momentum matching to free-space photons, that then travel through the electrode and are detected optically (pathway 1), in-plane mode overlap through the electrode (pathway 2), and mode overlap at the edge of the *M-I-M* TJ (pathway 3).

All pathways rely on near-field interactions of the *M-I-M* SPP with surface roughness that induces momentum matching with the daughter modes, but pathways 1 and 2 are especially sensitive to the attenuation by the metal electrode. This attenuation length has an exponential decay,

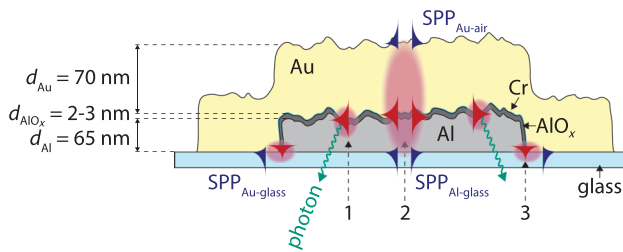


FIG. 2. The three main outcoupling pathways of the *M-I-M* SPP via scattering to photons (pathway 1), mode overlap and roughness-induced momentum matching through the electrodes (pathway 2) and mode overlap at the *M-I-M* TJ edge (pathway 3). The deposited thickness d of each layer is indicated, where d varies across the *M-I-M* TJ surface for each δ_q .

therefore a local difference of 10 nm in the electrode thickness due to surface roughness will have a large effect on the absorption of the evanescent field in the electrode. As we discuss below in detail, in systems with a large deviation in electrode thickness, this can result in certain areas with outcoupling efficiencies orders of magnitude larger than others. Moreover, when the thickness of the Al film is below Λ_{Al} , the metal becomes electromagnetically transparent, significantly reducing any attenuation of the evanescent field [61]. We note that plasmonic losses are large for thin metals, but here such “thin-area” defects are only local and will have only a small effect on the plasmonic properties of the entire film. Given the sensitivity of the momentum matching to d_{eff} we can then develop a finite-element-method (FEM) model to analyze the dependence of *M-I-M* SPP outcoupling on d_{eff} .

4. FEM modeling of *M-I-M* TJ

Using 2D FEM in COMSOL Multiphysics [51] we develop a two-step dipole model for analyzing the *M-I-M* SPP excitation and outcoupling efficiency in rough Au-AlO_x-Al *M-I-M* TJs and thus quantify the importance of d_{eff} (see Sec. S3 within the Supplemental Material for more details [26]). In the first step both Au and Al are assumed to extend to infinity. A dipole source at the center of the *M-I-M* TJ (oscillating normal to the *M-I-M* TJ interface) excites the *M-I-M* SPP mode, which subsequently dissipates within the metal electrodes. The time-averaged electromagnetic power $S = \frac{1}{2}\text{Re}(\mathbf{E} \times \mathbf{H}^*)$ crossing the *M-I-M* TJ boundary P_∞ is calculated and normalized by the *M-I-M* TJ surface area. In the second step we treat the thickness of the Al electrode as finite, so that the *M-I-M* SPP mode outcouples to photons or SPPs from the *M-I-M* TJ area. The Al electrode outcoupling power P_{Al} is calculated by integrating the Poynting vector \mathbf{S} across the Al-glass interface and normalizing with the *M-I-M* TJ area. The overall plasmon outcoupling efficiency η from the *M-I-M* TJ is evaluated as twice the ratio (since both top and bottom interfaces can be coupled to) of energy

converted as SPPs and photons to the total electromagnetic power generated within the *M-I-M* TJ (for a symmetrical system) and reported as a percentage:

$$\eta = 2 \frac{P_{\text{Al}}}{P_\infty} \times 100. \quad (10)$$

For ease of numerical convergence, we use a roughness profile represented by a 2D cross section of a statistically random surface $s(x, y)$:

$$s(x, y) = \sum_{-n}^{+n} \sum_{-m}^{+m} \aleph(n, m) \cos[2\pi(nx + my) + \phi(n, m)], \quad (11)$$

which can be described as a combination of multiple sinusoidal profiles with amplitude $\aleph(n, m)$ and random phase factor $\phi(n, m)$ [62]. Given this roughness model, we can now modify the analytical model for the LDOS of a smooth *M-I-M* TJ to also analytically model the LDOS of an *M-I-M* TJ with surface roughness.

5. SPP excitation in rough *M-I-M* TJs

The near-field interaction between a dipole source and roughness features can be approximated in terms of effective dipole moment μ_r and is equivalent to a current source, induced by the polarizability per unit area $h(\mathbf{r})$ [53]:

$$h(\mathbf{r}) = \sum_j \alpha_j \delta(\mathbf{r} - \mathbf{r}_j), \quad (12)$$

where α_j is the polarizability of the roughness feature at \mathbf{r}_j . We modify the dipole model (Eq. 1) for the near-field dipole-roughness interaction by considering roughness features as polarizable ellipsoids with the polarizability axis normal to the *M-I-M* TJ with an average polarizability per unit area $\langle h^2 \rangle$:

$$\langle h^2 \rangle^{1/2} = \frac{(c\varepsilon_1/3\pi)(\varepsilon_2 - \varepsilon_1)}{\varepsilon_1 + L(\varepsilon_2 - \varepsilon_1)}, \quad (13)$$

where L is the depolarization factor for an oblate spheroid [63]:

$$L = \frac{1 + e^2}{e^3}(e - \tan^{-1} e), \quad (14)$$

where $e = \sqrt{a^2/c^2 - 1}$ is the eccentricity and $a = b > c$ are the semiaxes of the ellipsoid. ε_1 and ε_2 correspond to the dielectric functions of the insulator and metal, respectively. In terms of the σ of the roughness features, the

effective magnitude of μ_r can be approximately written as [53]

$$|\mu_r| = \frac{64\pi \langle h^2 \rangle}{\varepsilon_1^2 \sigma^2}, \quad (15)$$

Modified dipole power dissipation is given by

$$\mathcal{P}_r = \frac{\omega}{2} \operatorname{Im}(\mu_r^* \cdot \mathbf{E}). \quad (16)$$

By calculating \mathcal{P}_r in Eq. (16) with experimentally derived roughness parameters (see Sec. II 2), we can conduct a quantitative analysis of the LDOS enhancement from the roughened electrodes and compare to experimental light-emission trends to corroborate the model.

B. Experiments

We fabricate *M-I-M* TJs with different δ_q to experimentally explore the change in outcoupling efficiency of the *M-I-M* SPP mode from light emission in the far field. Roughness parameters δ_q and σ for the fabricated *M-I-M* TJs used in the light-emission experiments are quantified with atomic force microscopy (AFM) analysis and used for the analytical modeling throughout the rest of this study.

1. M-I-M TJ fabrication

The *M-I-M* TJs are fabricated on borosilicate coverslips as previously reported using thermal evaporation of the bottom electrode, ambient oxidation of the Al to form the native oxide, and thermal evaporation of the top electrode with a 1-nm Cr adhesion layer [6]. All devices have the same top and bottom electrode thickness (70 ± 2 nm and 65 ± 2 nm, respectively), but we controlled the value of δ_q by controlling the wet-etching time of the Al electrode using tetramethylammonium hydroxide (TMAH; see Appendix A for details). We note that wet etching has been used often in the past to “roughen” the electrode and to enhance light emission from *M-I-M* TJs [3,15,35] without a quantitative characterization of the role of surface roughness in the enhancement.

2. Experimental determination of surface roughness

We perform AFM imaging with a fast-scan AFM scanner in tapping mode (Bruker, FastScan) over a $1 \times 1 \mu\text{m}$ area on each sample. Figures 3(a)–3(g) show the 2D surface topography for all *M-I-M* TJs from AFM imaging, with δ_q labeled for each, all scaled to the same height profile (given by the color bar on the right of the images). We determine the 2D roughness power spectral density (PSD) for each sample using the analysis software Nanoscope Analysis v1.8 to obtain the δ_q directly from the Fourier amplitude, and the PSD data is fitted with a *k*-correlation model [ABC model; Fig. 3(h)] to obtain σ [64]:

$$\Pi = \frac{A'}{(1 + B^2 f^2)^{(c+1)/2}}, \quad (17)$$

where Π represents the PSD, $A' = (1/2\sqrt{\pi})\{\Gamma[(C+1)/2]/\Gamma(C/2)\}(A \times B)$ and A , B , and C are fitting parameters with f representing the spatial frequency of surface features and Γ representing the gamma function. Figure 3(h) shows the raw data along with the fits to Eq. (17) (solid black lines)—raw data is shifted in the y axis for clarity. The value of σ is extracted from parameter B by $\sigma = B/2\pi$ [which is intrinsically related to the height-height correlation function $\langle \zeta(x)|\zeta(x+x') \rangle$, see Eq. (6)], and is listed alongside δ_q in Fig. 3(h). Figure 3(i) shows histograms of the grain widths for each δ_q using the data from Figs. 3(a)–3(g) along with the fit to a Gaussian distribution. From Fig. 3(i) we see that the Gaussian peak positions increase with increasing δ_q , implying that average grain width is increasing with increasing δ_q . The full width at half maximum of the Gaussian fits in Fig. 3(i) are used in Eqs. (14) to (16) as the semiaxis a and the δ_q values are used to represent the semiaxis c in the polarizability model to calculate the modified dipole power dissipation [Eq. (16)]. In total, we study seven different junctions with δ_q ranging from 3.4 to 14.3 nm and σ from 18.8 to 68.3 nm [Figs. 3(g)–3(i) inset]. From these results, we conclude that we are able to introduce a roughness varying from the electromagnetic screening length of the metal to an order of magnitude smaller than this screening length.

Surface-roughness-induced inhomogeneity results in a decrease of d_{eff} , which is smaller than the nominal film thickness, and with reduced electromagnetic attenuation—this coupling is especially efficient if the local roughness feature has a comparable size to the *M-I-M* SPP propagation length. Figure 3(j) shows a false-color cross-section scanning transmission electron microscopy (STEM) image of an Al-AlO_x-Au *M-I-M* TJ that has a large variation in electrode thickness due to roughness. In regions in the *M-I-M* TJ with local electrode thickness $0 < d_{\text{Al}} < \Lambda_{\text{Al}}$ (broken white circle 1), the mode overlap is almost par, whereas in regions where $d_{\text{Al}} > \Lambda_{\text{Al}}$ (dashed white circle 2) the outcoupling efficiency is orders of magnitude smaller.

3. Optical characterization

The electrical characteristics of the *M-I-M* TJs are given in Sec. S4 within the Supplemental Material [26] from which we conclude that the mechanism of charge transport is quantum-mechanical tunneling, similar to our previous works and that of others [1,6,65]. The optical properties of the *M-I-M* TJs are measured under an applied bias V_{bias} of -1.3 to -1.6 V, with an inverted microscope equipped with an electron multiplying CCD (EMCCD) and back-focal-plane (BFP) lens, which is

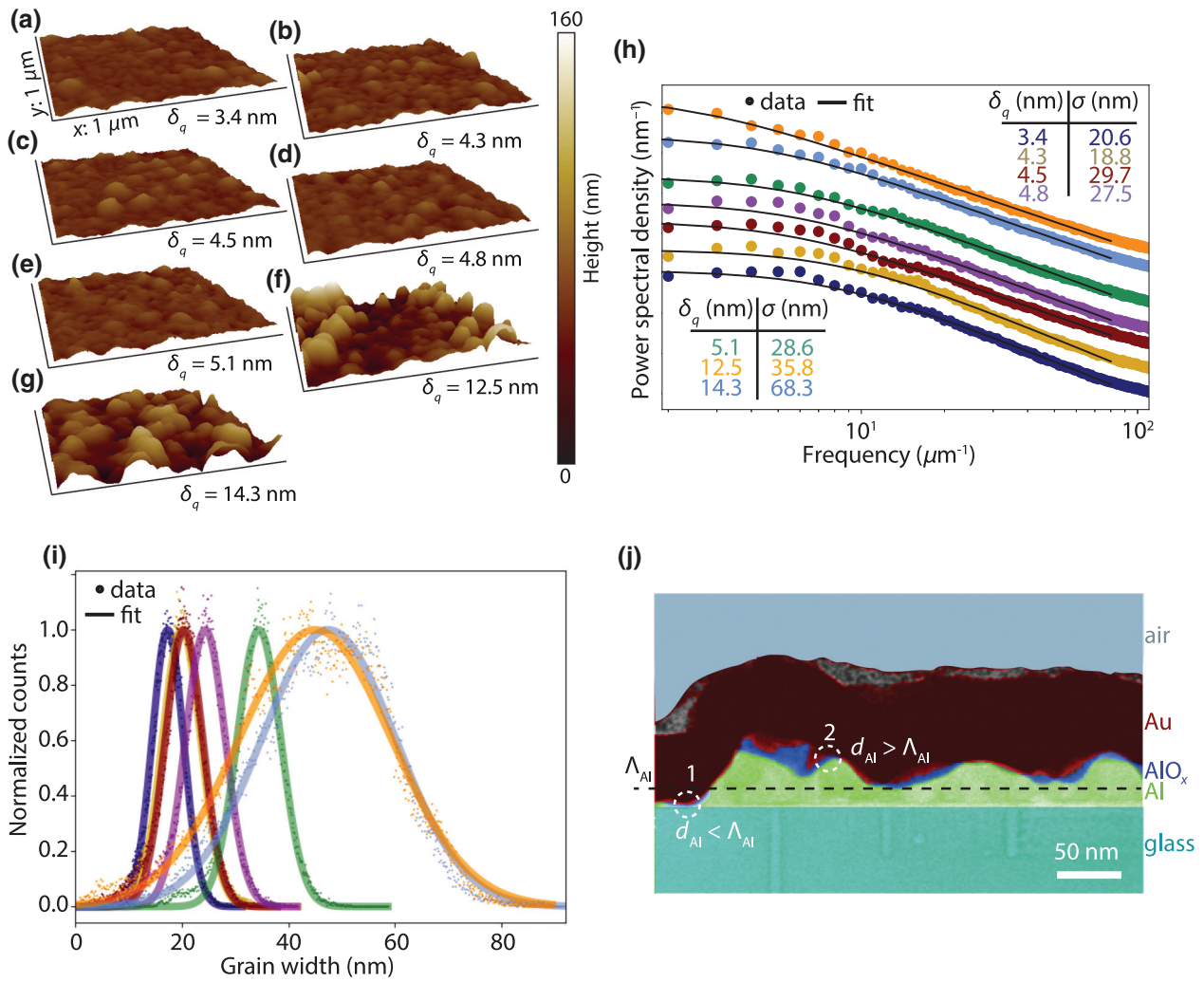


FIG. 3. (a)–(g) AFM images for all Al-AlO_x-Cr-Au *M-I-M* TJs with δ_q defined, all scaled equally, for $1 \times 1\text{-}\mu\text{m}$ images. (h) 2D PSD for the AFM surface topography shown in (a)–(g). Solid lines show the *k*-correlation fit [Eq. (17)] for 2D Fourier transform of the surface topography. Plots in PSD are vertically shifted to increase visibility; the inset summarizes the values of δ_q and σ for each device. (i) Grain width histograms (dots) and Gaussian fit (solid line) for each roughness value. (j) False color STEM image of the *M-I-M* TJ with changing Al thickness due to surface roughness.

described in detail in Appendix B and Ref. [1]. All experiments are carried out with a $100\times$ oil immersed lens with a numerical aperture of 1.49. Individual *M-I-M* TJs are biased and the light emanating from the *M-I-M* TJ is integrated over a period of time of 120 s. Figures 4(a) and 4(b) show the real-plane EMCCD images recorded from junctions with high ($\delta_q = 14.3$ nm, $V_{\text{bias}} = -1.6$ V) and low ($\delta_q = 3.4$ nm, $V_{\text{bias}} = -1.3$ V) δ_q values; Figs. 4(c) and 4(d) shows the corresponding BFP images (see Sec. S5 within the Supplemental Material [26] for all the corresponding EMCCD and BFP images of all *M-I-M* TJs, respectively). Different biases are applied as the voltage and corresponding current that light emission occurs at varies from device to device due to the inhomogeneity introduced from the wet etching, with all EMCCD image intensities normalized by current in our

analysis (see Sec. II C). The EMCCD images in Figs. 4(a) and 4(b) have the same intensity to compare *M-I-M* TJ light emission and scattering at the end of the waveguides. The intensities of the BFP images in Figs. 4(c) and 4(d) are chosen such to give the best contrast.

The real-plane EMCCD [Figs. 4(a) and 4(b)] images show that, for *M-I-M* TJs with low values of δ_q , light is emitted mainly from the *M-I-M* TJ edges (pathway 3) but for high values of δ_q light originates mainly from the *M-I-M* TJ area (pathway 1). This observation indicates that with increasing *M-I-M* TJ interface roughness, the efficiency of *M-I-M* SPP scattering into the radiative mode increases as the near-field interaction with the interface becomes stronger. For all devices, the scattered SPP modes are visible at the end of the Au waveguide; this

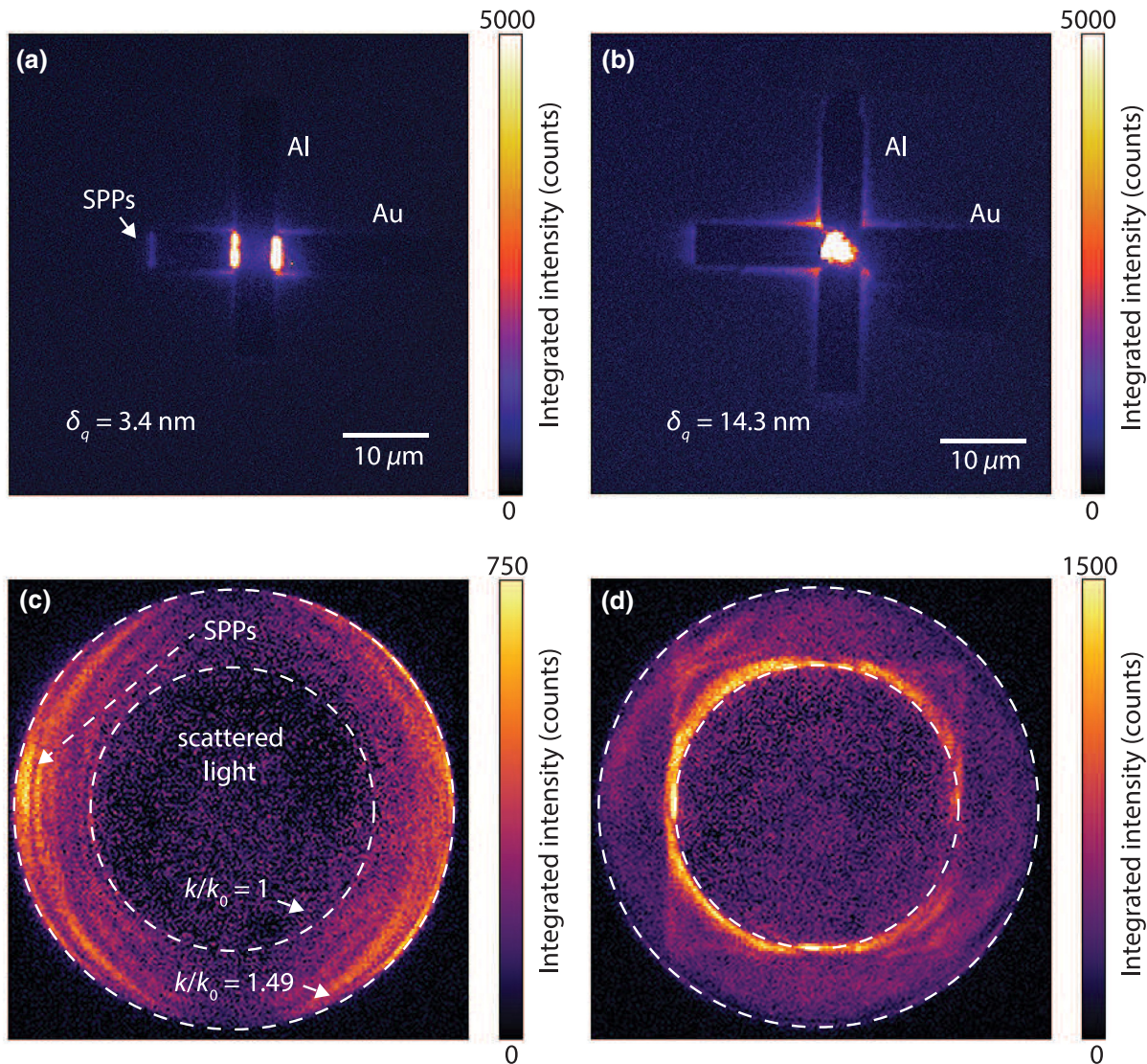


FIG. 4. (a),(b) Wide-field inverted optical microscopy images for the sample with (a) $\delta_q = 3.4 \text{ nm}$ and (b) $\delta_q = 14.3 \text{ nm}$, measured at $V_{\text{bias}} = -1.3 \text{ V}$ and $V_{\text{bias}} = -1.6 \text{ V}$, respectively. (c),(d) Corresponding BFP images, the inner white dashed line in the BFP refers to the critical angle of the total internal reflection at the air-glass interface ($k/k_0 = 1.0$); the outer white dashed line indicates the maximum angle of the collected light limited by the NA of the objective ($k/k_0 = 1.49$).

observation is corroborated by their presence in the BFP images, with intensity fringes detected between the outer ring corresponding to the NA of the objective ($k/k_0 = 1.49$) and when the normalized momentum is unity ($k/k_0 = 1$). Only scattered photons from the *M-I-M* TJ can be detected within $k/k_0 < 1$, whereas only scattered SPPs can be detected when $k/k_0 \geq 1$, which can be seen by the increase of intensity in the central ring. Figures 4(a) and 4(b) show that the light emission increases from the area of the *M-I-M* TJ relative to the edges as a function of δ_q , implying that the outcoupling efficiency of the *M-I-M* SPP mode by pathway 1 increases with increasing δ_q . This is further corroborated by the experimental BFP data [Figs. 4(c) and 4(d)] that shows sharp fringes for the SPP

compared to more diffuse light emission from the photonic contribution.

C. Discussions

Here we quantitatively investigate the role of surface roughness in outcoupling efficiency by analyzing the experimental results within the framework of FEM and the analytical LDOS model discussed in the theory, Sec. II 4–II 5. The key role played by d_{eff} in enhancing the outcoupling efficiency of a rough *M-I-M* TJ is analyzed using the 2D FEM modeling of the *M-I-M* TJ plasmonic response and is given in Figs. 5(a) and 5(b). Figure 5(a) shows the in-plane electric field distribution

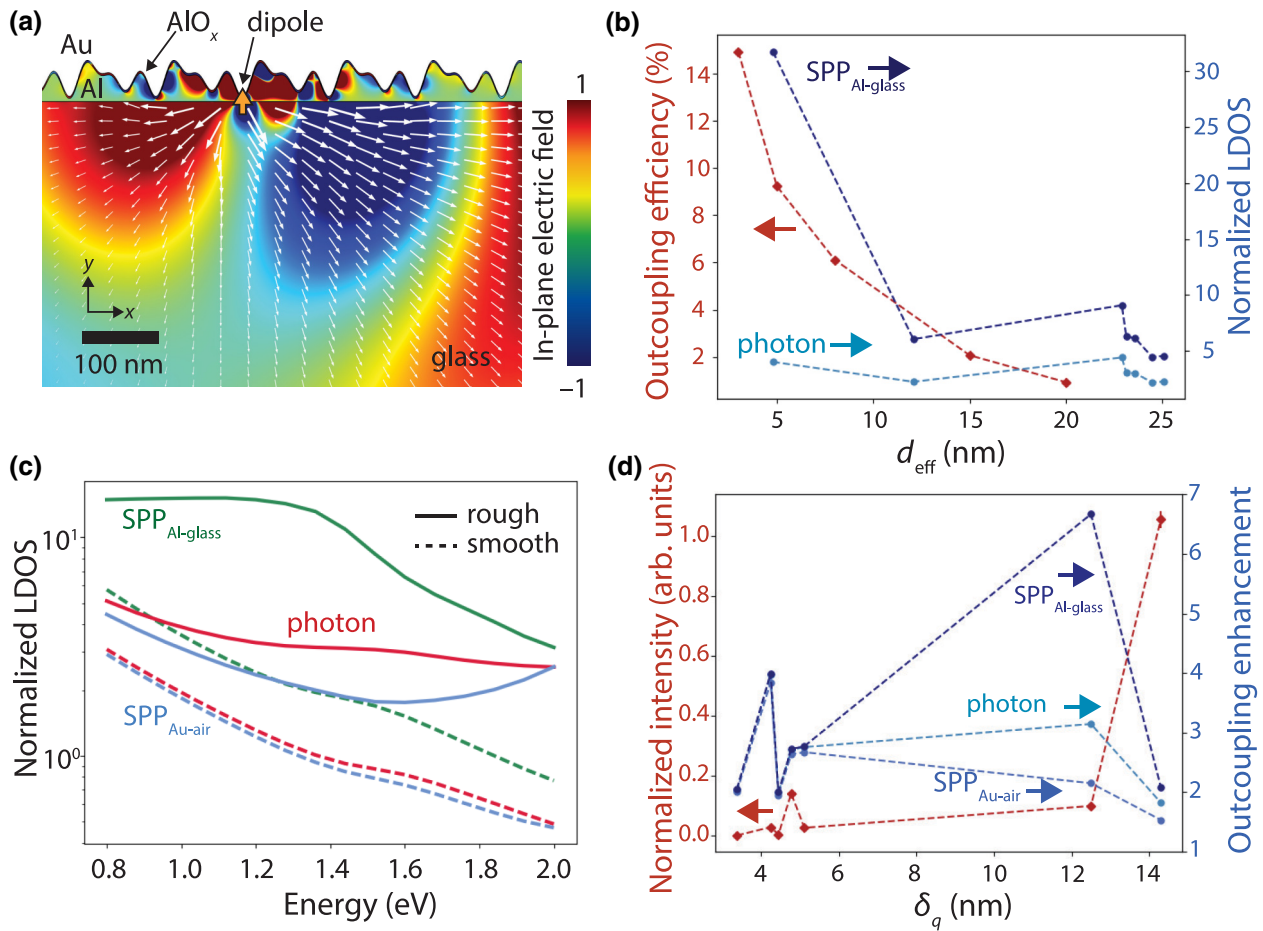


FIG. 5. (a) FEM modeling of *M-I-M* SPP mode outcoupling via the Al-glass interface for a rough junction. The dipole source is represented by the orange vertical arrow. The color map shows the simulated in-plane electric field E_y of the system. White arrows represent the electromagnetic power flow. (b) Outcoupling efficiency (calculated from the FEM model) as a function of d_{eff} of the Al electrode (left axis, with dashed red line as a visual guide) and the normalized LDOS [obtained from dipole power dissipation model—Eq. (16)] of the system for the SPP_{Al-glass} mode (dark blue, right axis) and radiative mode (light blue, right axis) evaluated at 1.37 eV. (c) Normalized LDOS as a function of energy for a smooth (dashed lines) and rough ($\delta_q = 3.4$ nm; solid lines) air-Au-AlO_x-Al-glass system for both SPP (Al-glass in green and Au-air in blue) and photon (red) emission. (d) Normalized experimental intensity as a function of device roughness (red; left axis) and the outcoupling enhancement $\mathcal{P}_r/\mathcal{P}$ from LDOS calculations as a function of roughness for the radiative and nonradiative modes (blue; right axis).

of the roughness-induced outcoupling of the *M-I-M* SPP mode. In Fig. 5(a), the Au electrode is assumed to be infinitely thick (represented by the Drude model) [57] so that outcoupling via the Au-air interface is completely absent to focus on the outcoupling via the Al-glass interface (since in our light-emission experiments, collection is performed from glass side only using high NA objective leakage radiation microscopy). The white arrows in Fig. 5(a) show the electromagnetic power flow from the *M-I-M* TJ through the Al-glass interface. The power flow has an asymmetry with respect to the location of the dipole due to the inhomogeneity of the roughness profile close to the excitation point. Figure 5(b) shows η [from Eq. (10)] as a function of d_{eff} of the Al electrode (on the left y axis). The calculated efficiency can be as high as 15% when $d_{\text{eff}} =$

3 nm, which is 6 orders of magnitude larger than hypothesized for outcoupling from idealized, flat junctions without roughness [2] and 2 orders of magnitude larger than we recently estimated using an *ad hoc* roughness profile [6]. Consequently, the overall electron-to-plasmon conversion efficiency $\eta_{\text{ep}} = 1.5\%$, which can be obtained from Fig. 5(b) for the specific roughness and effective thickness profile by multiplying η with theoretically predicted *M-I-M* SPP excitation efficiency approximately 10% [5], is in agreement with experimentally measured values [1,14].

In simulating the outcoupling efficiency of the *M-I-M* TJ in terms of *M-I-M* TJ plasmonic response, we restrict the modeling to 2D to circumvent the numerical convergence and meshing issues associated with a complex roughness topography. To gain more physical insight

for the roughness-enhanced outcoupling in *M-I-M* TJs, in terms of LDOS and experimentally obtained roughness parameters, we use the modified dipole power-dissipation model [Eq. (16)] with the roughness parameters readily available from the AFM analysis of *M-I-M* TJ devices (see Sec. II 2).

Figure 5(b) (right axis) shows the change in normalized LDOS with d_{eff} calculated for the rough case [Eq. (16), $\delta_q = 3.4 \text{ nm}$] and the trend is compared with the outcoupling efficiency obtained from the FEM modeling [Fig. 5(b), left axis]. The calculated LDOS of the photonic mode (light blue) and SPP_{Al-glass} (dark blue) is shown in Fig. 5(b) (right axis) for comparison. The near-field interaction of the *M-I-M* SPP with the interface does not result in equal outcoupling contributions to radiative and non-radiative modes. The outcoupling to the SPP_{Al-glass} mode is approximately $3 \times$ larger than to the photonic mode at $d_{\text{eff}} = 3 \text{ nm}$, which is due to the *M-I-M* SPP to SPP_{Al-glass} mode being a near-field to near-field interaction, compared to the far-field scattering of the *M-I-M* SPP to photons. This implies that not only are SPPs more likely to be excited than photons, but also using optical detection to measure the intensity underestimates the outcoupling to SPPs; these *M-I-M* TJs are better SPP sources than photon sources since light emission is less efficient than SPP excitation.

Figure 5(c) shows the impact of roughness in the normalized LDOS for a smooth *M-I-M* TJ ($\mathcal{P}/\mathcal{P}_0$, dashed lines) and for an *M-I-M* TJ with $\delta_q = 3.4 \text{ nm}$ ($\mathcal{P}_r/\mathcal{P}_0$, solid lines) as a function of energy, which are obtained from Eqs. (2) and (16), respectively. In short, surface roughness increases coupling to SPP modes (Al-glass in green and Au-air in blue) as well as the radiative mode (red) by modifying the LDOS, with preferential outcoupling to the SPP_{Al-glass} mode by around twice that of the radiative mode as discussed above. By using Eqs. (2) and (16) we can calculate the outcoupling enhancement (the ratio of the normalized LDOS $\mathcal{P}_r/\mathcal{P}$) between the rough and flat case for each sample and compare to experimentally measured light emission.

To meaningfully compare the experimentally measured emission intensity to theory, we normalize the light emission from the *M-I-M* TJ area. The total photon intensity of the scattered light ($k/k_0 < 1$) is measured from the BFP images for all *M-I-M* TJs of different roughness values since the BFP cleanly separates scattered light from leakage radiation [66], and then normalized to photon count per pixel per unit current and plotted [Fig. 5(d), left axis] against the theoretical calculation $\mathcal{P}_r/\mathcal{P}$ [Fig. 5(d), right axis].

Figure 5(d) shows two interesting trends: (i) as the roughness increases, light emission from the MIM-TJ area increases, and then saturates for $\delta_q > 5 \text{ nm}$, which is consistent with previous experimental observations [29]. Broadening of the *M-I-M* SPP mode dispersion due to

the decrease in effective thickness of the electrodes results in the observed saturation in emission intensity. (ii) We observe a local maximum in the emission intensity for $\delta_q \sim 5 \text{ nm}$, which is consistent with the LDOS calculations. This indicates that there is a preferential enhancement in the effective dipole amplitude with a local maximum in the ratio of $\langle h^2 \rangle$ to σ^2 [Eq. (15)] for a given *M-I-M* TJ. If we compare this trend with the outcoupling efficiency plot in Fig. 5(b) calculated from the FEM model, which shows a monotonic increase with reduced effective thickness, we conclude that in the FEM model the outcoupling mechanism is mainly dominated by the near-field interaction between the source dipole and the roughness features. In the analytical LDOS calculations, however, the effective dipole amplitude [Eq. (15)] takes not only the roughness into account, but also the average polarizability per unit area, which explicitly depends on the grain size distribution [see Fig. 3(i)] at the electrode surface. This effective medium approach qualitatively replicates the observed trend and local maximum in the emission enhancement with roughness. Therefore, the local maximum can be attributed to an optimum roughness distribution resulting in an effective electrode thickness maximizing the outcoupling efficiency.

At extremely high roughness values of $\delta_q > 12 \text{ nm}$, the experimental data deviates from the theory (seen from the increase in the trend of the experimental data but decrease in the LDOS enhancement). For a highly rough *M-I-M* TJ [$\delta_q \sim 14.5 \text{ nm}$, Fig. 3(i)], the effective thickness of the electrodes becomes extremely small compared to the skin depth of the metal and the electromagnetic properties of the metal electrode begin to mimic those of an array of nanoscale grains rather than a continuous film [see Eq. (9)]. From Eq. (8) for large values of σ , the surface grain dispersion is larger than the propagation length of the *M-I-M* SPP L_{M-I-M} SPP (see Sec. S1 within the Supplemental Material for details [26]) and there are no significant scatterers for the *M-I-M* SPP to interact with. In contrast, when $\sigma \rightarrow 0$ the entire film behaves as a highly dense array of scatterers, causing high scattering and thus a high enhancement of 2 orders of magnitude (see Fig. 6 for the discussion). This is equivalent to the Purcell effect in plasmonic cavities due to the presence of a highly dense array of noninteracting nanoantennas [67]. These two effects define the limit of the LDOS enhancement calculation observed as the downturn in Fig. 5(d) (see Sec. S6 within the Supplemental Material [26]).

To further understand the interplay between δ_q and σ , we analyze the outcoupling enhancement $\mathcal{P}_r/\mathcal{P}$ as a function of both parameters against the effective mode index (k/k_0) (Fig. 6) at $\lambda_d = 900 \text{ nm}$. For both plots, the following features are observed around SPP modes at the air and glass interfaces (effective index of 1 and 1.52, respectively). In Fig. 6(a), as δ_q increases for a fixed $\sigma = 35 \text{ nm}$, $\mathcal{P}_r/\mathcal{P}$ increases by 2 orders of magnitude, with an upper

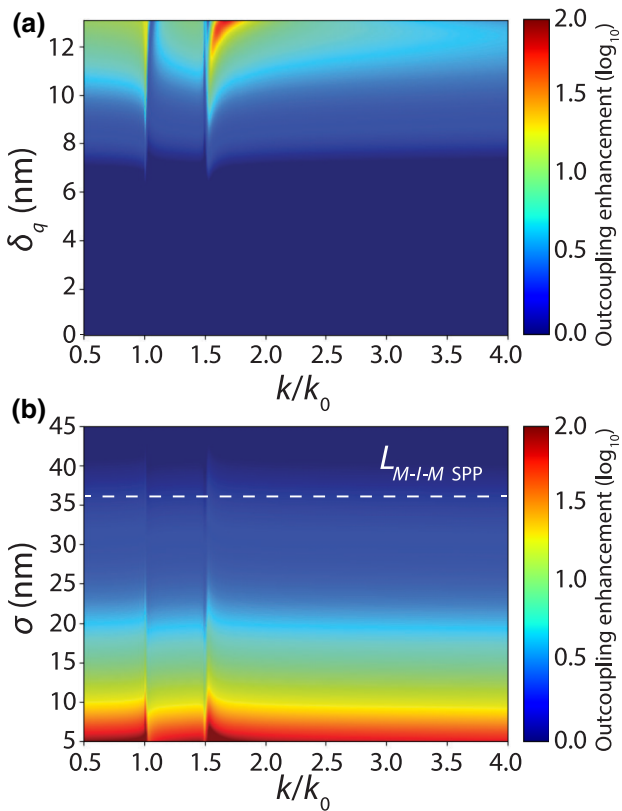


FIG. 6. Heat maps showing the outcoupling enhancement $\mathcal{P}_r/\mathcal{P}$ as a function of (a) δ_q vs k/k_0 and (b) σ vs k/k_0 (calculated at $\lambda_d = 900$ nm), where $L_{M-I-M \text{ SPP}}$ is indicated by the white dashed line. Note the intensity bar is in logarithmic scale.

bound where the roughened film turns into an array of nanoscale holes. Figure 6(b) shows $\mathcal{P}_r/\mathcal{P}$ evaluated as a function of k/k_0 and σ for $\delta_q = 4.3$ nm and the enhancement of 2 orders of magnitude in $\mathcal{P}_r/\mathcal{P}$ decreases with increasing σ . We indicate $L_{M-I-M \text{ SPP}}$ with a white dashed line to confirm that, for $\sigma > L_{M-I-M \text{ SPP}}$, there is no significant outcoupling enhancement. These calculations not only elucidate the interplay between δ_q and σ , which also explain the experimental peak seen in Fig. 5(d), but uncover competing effects that could be exploited by carefully designed metasurfaces. Instead of randomly roughening these systems to gain an average effect, a purposely designed metasurface could be built around the optimal combination of δ_q and σ and integrated into $M-I-M$ TJs to attain higher efficiency than statistical roughening, and by designing metasurfaces that can tune σ to move from the continuous film limit to nanoscatterers with different height and periodicity, could also enable selective mode excitation.

III. CONCLUSIONS

In this work we develop a mathematical framework to describe surface roughness in $M-I-M$ TJs and use it to

explore outcoupling efficiencies of the $M-I-M$ SPP mode to single-interface SPP modes and photons. We formulate a phenomenological model for the LDOS and mode dispersion of a roughened $M-I-M$ TJ, by exploring the near-field coupling of the $M-I-M$ SPP to radiative and nonradiative modes. By FEM modeling of the $M-I-M$ SPP excitation in the roughened $M-I-M$ TJ, we show that outcoupling efficiency can be as high as 15% for effective thicknesses of 3 nm, giving total electron-to-SPP conversion efficiencies $> 1\%$ (when multiplied with the internal quantum efficiency of the $M-I-M$ TJ), which corroborates recent experimental results demonstrating total device efficiencies of 0.1% [1,6]. We demonstrate that two competing physical parameters δ_q and σ can also lead to optimal outcoupling (in this work for $\delta_q \approx 5$ nm).

This work explores the near-field interaction of the $M-I-M$ SPP mode with nonradiative and radiative daughter modes, emphasizing the crucial role that surface roughness can play in $M-I-M$ TJs. Here we highlight the importance of the contribution of all outcoupling pathways to interface SPP excitation—especially from direct scattering to photons as roughness increases—unlike previous works [2,23] that only considered excitation from the edge of the $M-I-M$ TJ (pathway 3). While this study focuses on the $M-I-M$ SPP outcoupling, the theoretical analysis presented here could also be further expanded by incorporating the effect of $M-I-M$ TJ roughness on theories for inelastic tunneling of electrons [68] to explore the upper limit of plasmon excitation efficiency in large area $M-I-M$ TJs. This work establishes theoretically the high observed experimental efficiencies of $M-I-M$ TJs as electrical SPP sources, and posits that further optimization potentially can improve efficiencies.

ACKNOWLEDGMENTS

The authors acknowledge the National Research Foundation (NRF) for supporting this research under the Prime Minister's Office, Singapore, under its Medium Sized Centre Programme and the Competitive Research Programme (CRP) (NRF-CRP17-2017-08). The authors also thank Centre for Advanced 2D Materials (CA2DM) for the provided facilities. All authors thank Professor José Carlos Viana Gomes for his valuable insights into light-matter interactions with surface roughness.

T.J. Duffin and V. Kalathingal contributed equally to this work.

APPENDIX A: DEVICE FABRICATION

All devices are fabricated using a similar method to our previous work [1] on borosilicate coverslips (Paul Marienfeld GmbH, 22 × 22 mm, 0.16–0.19 mm thick). Contact pads (100 × 100 μm) are patterned using a laser-writer (Microtech, LW405B), with bilayer resist with a total resist thickness of approximately 1.3 μm : LOR

3A, (prebake at 170 °C for 5 min) and S1805 (prebake at 115 °C for 1 min) exposed with a 405-nm beam at 320 mJ/cm², before electron-beam deposition (AJA) of the bimetal layer of Ti/Au (3/30 nm) with Ti as the adhesion layer. After liftoff, the bottom electrode is patterned by electron-beam lithography (JEOL, JBX-6300FS), using bilayer PMMA A3 495/A5 950 resist (MicroChem, prebake at 180 °C for 5/2 min) and exposed with a 5-nA current. After development in MIBK 1:3 IPA, Al is deposited by thermal evaporation (Kurt J. Lesker, NANO 36) at 1 nm/s for a final thickness of 45 nm. Finally, the top electrodes are patterned exposed using electron-beam lithography again with the same parameters.

After resist development, the samples are immersed into MF-319 optical developer, with active ingredient TMAH, which is an Al etchant, to remove AlO_x for 20 s and rinsed with water for 1 min. Etching thins the Al electrodes in the region under the top electrode, so that the final thickness in the *M-I-M* TJ area ($5 \times 5 \mu\text{m}^2$) is $d_{\text{Al}} = 40 \text{ nm}$. Fresh native AlO_x is then grown in ambient conditions for 2 h, before the Au layer with 1 nm of Cr adhesion layer is deposited using a thermal evaporation again to a thickness 60 nm. Cr here allows better adhesion of the Au to the AlO_x as cleaner liftoff, as well as smooth film formation as can be seen from the AFM and STEM images [Figs. 3(a)–3(g) and 3(j)]. Due to the high deposition rate of Al, coupled with the wet etching, significant inhomogeneity in surface roughness across the sample is evident; this is used to obtain different *M-I-M* TJs with different roughness conditions by simply controlling the immersion time and thus the etching rate of Al in TMAH.

APPENDIX B: OPTICAL SETUP

Optical light-emission measurements are performed with an inverted microscope system (Nikon Eclipse Ti-E) using a 100× oil objective (Numerical Aperture, NA = 1.49) collected by both a spectrometer with a Si-based detector and wavelength range 400–1100 nm (Andor, Shamrock 122 303i) and an electron multiplying CCD (EMCCD, iXon Ultra 897). Both real and BFP images are taken with the EMCCD, with a BFP lens placed at the Fourier plane of the optical path to project the BFP onto the EMCCD.

- [1] W. Du, T. Wang, H.-S. Chu, and C. A. Nijhuis, Highly efficient on-chip direct electronic-plasmonic transducers, *Nat. Photonics* **11**, 623 (2017).
- [2] M. Parzefall and L. Novotny, Light at the end of the tunnel, *ACS Photonics* **5**, 4195 (2018).
- [3] J. Lambe and S. L. McCarthy, Light Emission from Inelastic Electron Tunneling, *Phys. Rev. Lett.* **37**, 923 (1976).
- [4] Z. Szentirmay, Surface plasmon assisted electron-photon interaction in metal-oxide-metal layered structures, *Prog. Quantum Electron.* **15**, 175 (1991).
- [5] L. C. Davis, Theory of surface-plasmon excitation in metal-insulator-metal tunnel junctions, *Phys. Rev. B* **16**, 2482 (1977).
- [6] K. S. Makarenko, T. X. Hoang, T. J. Duffin, A. Radulescu, V. Kalathingal, H. J. Lezec, H.-S. Chu, and C. A. Nijhuis, Efficient surface plasmon polariton excitation and control over outcoupling mechanisms in metal–insulator–metal tunneling junctions, *Adv. Sci.* **7**, 1900291 (2020).
- [7] G. A. Lopez, M.-C. Estevez, M. Soler, and L. M. Lechuga, Recent advances in nanoplasmonic biosensors: Applications and lab-on-a-chip integration, *Nanophotonics* **6**, 123 (2017).
- [8] J. Langer, S. M. Novikov, and L. M. Liz-Marzán, Sensing using plasmonic nanostructures and nanoparticles, *Nanotechnology* **26**, 322001 (2015).
- [9] T. Harter, S. Muehlbrandt, S. Ummethala, A. Schmid, S. Nellen, L. Hahn, W. Freude, and C. Koos, Silicon–plasmonic integrated circuits for terahertz signal generation and coherent detection, *Nat. Photonics* **12**, 625 (2018).
- [10] W. Li and J. G. Valentine, Harvesting the loss: Surface plasmon-based hot electron photodetection, *Nanophotonics* **6**, 177 (2017).
- [11] C. Haffner, W. Heni, Y. Fedoryshyn, J. Niegemann, A. Melikyan, D. L. Elder, B. Baeuerle, Y. Salamin, A. Josten, U. Koch, C. Hoessbacher, F. Ducry, L. Juchli, A. Emboras, D. Hillerkuss, M. Kohl, L. R. Dalton, C. Hafner, and J. Leuthold, All-plasmonic Mach–Zehnder modulator enabling optical high-speed communication at the microscale, *Nat. Photonics* **9**, 525 (2015).
- [12] T. J. Duffin, M. P. Nielsen, F. Diaz, S. Palomba, S. A. Maier, and R. F. Oulton, Degenerate four-wave mixing in silicon hybrid plasmonic waveguides, *Opt. Lett.* **41**, 155 (2016).
- [13] M. P. Nielsen, X. Shi, P. Dichtl, S. A. Maier, and R. F. Oulton, Giant nonlinear response at a plasmonic nanofocus drives efficient four-wave mixing, *Science* **358**, 1179 (2017).
- [14] H. Qian, S.-W. Hsu, K. Gurunatha, C. T. Riley, J. Zhao, D. Lu, A. R. Tao, and Z. Liu, Efficient light generation from enhanced inelastic electron tunnelling, *Nat. Photonics* **12**, 485 (2018).
- [15] P. Dawson, D. G. Walmsley, H. A. Quinn, and A. J. L. Ferguson, Observation and explanation of light-emission spectra from statistically rough Cu, Ag, and Au tunnel junctions, *Phys. Rev. B* **30**, 3164 (1984).
- [16] D. P. Siu and T. K. Gustafson, Stimulated emission of surface plasmons by electron tunneling in metal-barrier-metal structures, *Appl. Phys. Lett.* **32**, 500 (1978).
- [17] F. J. G. de Abajo and M. Kociak, Probing the Photonic Local Density of States with Electron Energy Loss Spectroscopy, *Phys. Rev. Lett.* **100**, 106804 (2008).
- [18] T. V. Shahbazyan, Local Density of States for Nanoplasmonics, *Phys. Rev. Lett.* **117**, 207401 (2016).
- [19] R. Esteban, A. G. Borisov, P. Nordlander, and J. Aizpurua, Bridging quantum and classical plasmonics with a quantum-corrected model, *Nat. Commun.* **3**, 825 (2012).

- [20] J. Aizpurua, G. Hoffmann, S. P. Apell, and R. Berndt, Electromagnetic Coupling on an Atomic Scale, *Phys. Rev. Lett.* **89**, 156803 (2002).
- [21] H. Xu, J. Aizpurua, M. Käll, and P. Apell, Electromagnetic contributions to single-molecule sensitivity in surface-enhanced Raman scattering, *Phys. Rev. E* **62**, 4318 (2000).
- [22] D. L. Mills, M. Weber, and B. Laks, in *Tunneling Spectroscopy* (Springer, USA, 1982), p. 121.
- [23] M. Parzefall, P. Bharadwaj, A. Jain, T. Taniguchi, K. Watanabe, and L. Novotny, Antenna-coupled photon emission from hexagonal boron nitride tunnel junctions, *Nat. Nanotechnol.* **10**, 1058 (2015).
- [24] J. F. Donohue and E. Y. Wang, Surface plasmon dispersion analysis in the metal-oxide-metal tunnel diode, *J. Appl. Phys.* **62**, 1313 (1987).
- [25] A. Takeuchi, J. Watanabe, Y. Uehara, and S. Ushioda, Prism-coupled light emission from tunnel junctions containing interface roughness: Theory, *Phys. Rev. B* **38**, 12948 (1988).
- [26] See Supplemental Material at <http://link.aps.org/supplemental/10.1103/PhysRevApplied.14.044021> for more details on surface plasmon polariton propagation length [69–72] (Sec. I), local density of optical states' calculations (Sec. II), finite-element modeling with COMSOL Multiphysics (Sec. III), electrical characterization of the devices [73] (Sec. IV), optical measurements (Sec. V), and a discussion on the ratio of grain size distribution to the transverse correlation length (Sec. VI).
- [27] M. Hanisch and A. Otto, Light emission from rough tunnel junctions in UHV, *J. Phys.: Condens. Matter* **6**, 9659 (1994).
- [28] J. Soole and H. Hughes, Roughness-coupled light emission from tunnel junctions: The role of the fast surface plasmon, *Surf. Sci.* **197**, 250 (1988).
- [29] S. L. McCarthy and J. Lambe, Enhancement of light emission from metal-insulator-metal tunnel junctions, *Appl. Phys. Lett.* **30**, 427 (1977).
- [30] A. Adams and P. K. Hansma, Light emission from small metal particles and thin metal films excited by tunneling electrons, *Phys. Rev. B* **23**, 3597 (1981).
- [31] K. Parvin and W. Parker, Optical spectra and angular dependence of the visible light emitted by metal-insulator-metal tunnel junctions, *Solid State Commun.* **37**, 629 (1981).
- [32] J. F. Donohue and E. Y. Wang, Observation of radiative surface plasmons in metal-oxide-metal tunnel junctions, *J. Appl. Phys.* **59**, 3137 (1986).
- [33] P. Dawson and D. Walmsley, Light emission from statistically rough Ag tunnel junctions, *Surf. Sci.* **171**, 146 (1986).
- [34] P. Dawson and D. Walmsley, Light emission from nominally smooth Ag tunnel junctions, *Surf. Sci.* **171**, 135 (1986).
- [35] P. D. Sparks and J. E. Rutledge, Light emission from randomly rough tunnel junctions, *Phys. Rev. B* **40**, 7574 (1989).
- [36] K. Suzuki, J. Watanabe, A. Takeuchi, Y. Uehara, and S. Ushioda, Two-mode radiation from light-emitting tunnel junctions with surface roughness, *Solid State Commun.* **69**, 35 (1989).
- [37] M. J. Bloemer, J. G. Mantovani, J. P. Goudonnet, D. R. James, R. J. Warmack, and T. L. Ferrell, Observation of driven surface-plasmon modes in metal particulates above tunnel junctions, *Phys. Rev. B* **35**, 5947 (1987).
- [38] J. Kirtley, T. Theis, and J. Tsang, Light emission from tunnel junctions on gratings, *Phys. Rev. B* **24**, 5650 (1981).
- [39] P. D. Sparks, T. Sjodin, B. W. Reed, and J. Stege, Light Emission from the Slow Mode of Tunnel Junctions on Short Period Diffraction Gratings, *Phys. Rev. Lett.* **68**, 2668 (1992).
- [40] S. Ushioda, Y. Uehara, M. Takada, K. Otsubo, and J. Murota, Grating-coupled light emission from the slow mode of metal-insulator-metal tunnel junctions, *Jpn. J. Appl. Phys.* **31**, L870 (1992).
- [41] J. R. Kirtley, T. N. Theis, and J. C. Tsang, Diffraction-grating-enhanced light emission from tunnel junctions, *Appl. Phys. Lett.* **37**, 435 (1980).
- [42] A. Köck, W. Beinstingl, K. Berthold, and E. Gornik, Surface plasmon polariton enhanced light emission from schottky diodes, *Appl. Phys. Lett.* **52**, 1164 (1988).
- [43] S. Ushioda, J. Rutledge, and R. Pierce, Prism-Coupled Light Emission from Tunnel Junctions, *Phys. Rev. Lett.* **54**, 224 (1985).
- [44] S. Ushioda, Light emission associated with tunneling phenomena, *J. Lumin.* **47**, 131 (1990).
- [45] A. Kolomenski, A. Kolomenskii, J. Noel, S. Peng, and H. Schuessler, Propagation length of surface plasmons in a metal film with roughness, *Appl. Opt.* **48**, 5683 (2009).
- [46] L. Jiang, T. Wang, and C. A. Nijhuis, Fabrication of ultra-flat silver surfaces with sub-micro-meter scale grains, *Thin Solid Films* **593**, 26 (2015).
- [47] S. J. Henley, J. D. Carey, and S. R. P. Silva, Pulsed-laser-induced nanoscale island formation in thin metal-on-oxide films, *Phys. Rev. B* **72**, 195408 (2005).
- [48] F. Benz, M. K. Schmidt, A. Dreismann, R. Chikkaraddy, Y. Zhang, A. Demetriadou, C. Carnegie, H. Ohadi, B. de Nijs, R. Esteban, J. Aizpurua, and J. J. Baumberg, Single-molecule optomechanics in “picocavities”, *Science* **354**, 726 (2016).
- [49] M. Urbieto, M. Barbry, Y. Zhang, P. Koval, D. Sánchez-Portal, N. Zabala, and J. Aizpurua, Atomic-scale lightning rod effect in plasmonic picocavities: A classical view to a quantum effect, *ACS Nano* **12**, 585 (2018).
- [50] Y. Zhao, X. Liu, D. Y. Lei, and Y. Chai, Effects of surface roughness of Ag thin films on surface-enhanced Raman spectroscopy of graphene: Spatial nonlocality and physisorption strain, *Nanoscale* **6**, 1311 (2014).
- [51] COMSOL Inc., Comsol multiphysics.
- [52] L. Novotny and B. Hecht, *Principles of Nano-Optics* (Cambridge University Press, New York, 2012).
- [53] G. Ford and W. Weber, Electromagnetic interactions of molecules with metal surfaces, *Phys. Rep.* **113**, 195 (1984).
- [54] B. Laks and D. Mills, Roughness and the mean free path of surface polaritons in tunnel-junction structures, *Phys. Rev. B* **21**, 5175 (1980).
- [55] A. Sobhani, A. Manjavacas, Y. Cao, M. J. McClain, F. J. G. de Abajo, P. Nordlander, and N. J. Halas, Pronounced linewidth narrowing of an aluminum nanoparticle plasmon resonance by interaction with an aluminum metallic film, *Nano Lett.* **15**, 6946 (2015).

- [56] N. Kroó, Z. Szentirmay, and J. Félszerfalvi, Optical determination of mean free path of hot electrons in metals, *Phys. Status Solidi B* **102**, 227 (1980).
- [57] R. L. Olmon, B. Slovick, T. W. Johnson, D. Shelton, S.-H. Oh, G. D. Boreman, and M. B. Raschke, Optical dielectric function of gold, *Phys. Rev. B* **86**, 235147 (2012).
- [58] D. L. Mills and A. A. Maradudin, Surface roughness and the optical properties of a semiinfinite material the effect of a dielectric overlayer, *Phys. Rev. B* **12**, 2943 (1975).
- [59] A. A. Maradudin and T. Michel, The transverse correlation length for randomly rough surfaces, *J. Stat. Phys.* **58**, 485 (1990).
- [60] T. S. Rahman and A. A. Maradudin, Effect of surface roughness on the image potential, *Phys. Rev. B* **21**, 504 (1980).
- [61] F. Abelès, *Optical Properties of Solids* (North-Holland Pub. Co., Amsterdam, 1972).
- [62] COMSOL Blog, www.comsol.com/blogs.
- [63] L. D. Landau, *Electrodynamics of Continuous Media* (Elsevier, Great Britain, 2013).
- [64] Y. Gong, S. T. Misture, P. Gao, and N. P. Mellott, Surface roughness measurements using power spectrum density analysis with enhanced spatial correlation length, *J. Phys. Chem. C* **120**, 22358 (2016).
- [65] J. G. Simmons, Generalized formula for the electric tunnel effect between similar electrodes separated by a thin insulating film, *J. Appl. Phys.* **34**, 1793 (1963).
- [66] T. Wang, B. Rogez, G. Comtet, E. Le Moal, W. Abidi, H. Remita, G. Dujardin, and E. Boer-Duchemin, Scattering of electrically excited surface plasmon polaritons by gold nanoparticles studied by optical interferometry with a scanning tunneling microscope, *Phys. Rev. B* **92**, 045438 (2015).
- [67] J. J. Baumberg, J. Aizpurua, M. H. Mikkelsen, and D. R. Smith, Extreme nanophotonics from ultrathin metallic gaps, *Nat. Mater.* **18**, 668 (2019).
- [68] V. A. Shkoldin, D. V. Permyakov, K. S. Ladutenko, M. V. Zhukov, A. A. Vasiliev, A. O. Golubok, A. V. Uskov, A. D. Bolshakov, A. A. Bogdanov, A. K. Samusev, and I. S. Mukhin, Crucial role of metal surface morphology in photon emission from a tunnel junction at ambient conditions, *J. Phys. Chem. C* **123**, 8813 (2019).
- [69] S. A. Maier, *Plasmonics: Fundamentals and Applications* (Springer, New York, USA, 2007).
- [70] S. I. Bozhevolnyi and T. Søndergaard, General properties of slow-plasmon resonant nanostructures: Nano-antennas and resonators, *Opt. Express* **15**, 10869 (2007).
- [71] P. B. Johnson and R. W. Christy, Optical constants of the noble metals, *Phys. Rev. B* **6**, 4370 (1972).
- [72] K. M. McPeak, S. V. Jayanti, S. J. P. Kress, S. Meyer, S. Iotti, A. Rossinelli, and D. J. Norris, Plasmonic films can easily be better: Rules and recipes, *ACS Photonics* **2**, 326 (2015).
- [73] W. F. Brinkman, R. C. Dynes, and J. M. Rowell, Tunneling conductance of asymmetrical barriers, *J. Appl. Phys.* **41**, 1915 (1970).